Investigating the feasibility of a hand-held photoacoustic imaging probe for margin assessment during breast conserving surgery

E. Rascevska [a,b], L.C.M. Yip [a,e], P. Omidi [a,b], M. Brackstone [c,d], J.J.L. Carson [a,b,c,e,*]

[a] *Imaging Program, Lawson Health Research Institute, 268 Grosvenor St., London N6A 4V2, ON, Canada*
[b] *School of Biomedical Engineering, Western University, 1151 Richmond St., London N6A 3K7, ON, Canada*
[c] *Department of Surgery, Schulich School of Medicine and Dentistry, Western University, 1151 Richmond St., London N6A 3K7, ON, Canada*
[d] *Department of Oncology, Schulich School of Medicine & Dentistry, The University of Western Ontario, 1151 Richmond St., N6A 3K7, London, ON, Canada*
[e] *Department of Medical Biophysics, Schulich School of Medicine and Dentistry, Western University, 1151 Richmond St., London N6A 3K7, ON, Canada*

ARTICLE INFO

ABSTRACT

Approximately 19 % of breast cancer patients undergoing breast conserving surgery (BCS) must return for a secondary surgery due to incomplete tumour removal. Our previous work demonstrated that the lower lipid content, characteristic of tumour tissue, was observed as regions of hypo-intense photoacoustic (PA) contrast. The goal of this work was to evaluate feasibility of a low-frequency, hand-held PA imaging probe for surgical margin assessment based on lipid content differences. Here, we describe (i) the design of a prototype hand-held PA imaging probe, (ii) the effect of limited-bandwidth on image contrast, (iii) accuracy towards hypo-intense contrast detection, (iv) the limited-view characteristics of the single sensor design, and (iv) early imaging results of an ex-vivo breast cancer specimen. The probe incorporates a single polyvinylidene fluoride acoustic sensor, a 1-to-4 optical fibre bundle and a polycarbonate axicon lens for light delivery. Imaging results on phantoms designed to mimic positive margins demonstrated the ability to detect gaps in optical absorption as small as 1 mm in width. Compared to images from a near full-view PAI system, the hand-held PAI probe had higher signal to noise ratio but suffered from negativity image artifacts. Lumpectomy specimen imaging showed that strong signals can be obtained from the fatty tissue. Taken together, the results show this imaging approach with a hand-held probe has potential for detection of residual breast cancer tissue during BCS; however, more work is needed to reduce the size of the probe to fit within the surgical cavity.

1. Introduction

Approximately 60–70 % of breast cancer patients, typically with stage I or II cancer, undergo breast conserving surgery (BCS) along with adjuvant therapy [1]. The goal of BCS is to excise all tumour tissue together with a margin of healthy tissue while maintaining the cosmetic appearance of the breast. The excision is considered successful if margin status is reported negative by pathology and is associated with reduced local recurrence. A surgery is considered a failure if the margin status is reported positive. Current guidelines for invasive breast cancer recommend that no tumour cells be detected on the surface of excised tissue [2–4]. For ductal carcinoma in situ (DCIS), the criterion for a negative assessment is a minimum 2 mm margin of healthy tissue at the surface [2–4].

While pathology is a well-established method for margin assessment,

surgeons do not receive real-time feedback and margin status is reported only a few days post-surgery. In case of positive margin status, the patient may need to return for a re-excision surgery to remove the residual tumour tissue. Failure rates vary between surgeons and across health care institutions, but on average patients need to return for a re-excision surgery in 19 % of cases [5,6]. Re-excision surgeries delay adjuvant therapy delivery, degrade cosmetic outcome, and increase the likelihood for complications.

In an effort to provide feedback during surgery, several methods have been proposed including imprint cytology, frozen-section analysis, ultrasound, X-ray imaging, and Raman spectroscopy [7–11]. Most of these techniques are performed on the *ex vivo* specimen rather than inside the surgical cavity. As such, they tend to prolong BCS and create an extra challenge for the surgeon, since it is often difficult to relate a position on the specimen to its associated position inside the surgical

---

cavity.

Inspection of the surgical cavity, as opposed to the specimen, can provide the surgeon with a precise location of cancerous tissue. Three devices are currently under investigation for intracavity use. ClearEdge (LSBioPath, Saratoga, CA, USA) and MarginProbe® (Dilon Technologies® Inc., Newport News, VA, USA) use radio frequency (RF) spectroscopy. ClearEdge has sensitivity and specificity of 87.3 % and 75.6 %, respectively, whereas MarginProbe® reported 70 % sensitivity and 70 % specificity for binary differentiation of cancerous vs healthy tissue with features as small as 0.15 mm, and 100 % sensitivity, 87 % specificity for tissue with feature sizes of a few mm [12,13]. The intelligent knife (iKnife) (Waters Corporation, Milford, MA, USA) analyses aerosols released during electrosurgical dissection utilising rapid evaporative ionization mass spectrometry. Binary tissue classification was estimated to have 97.7 % specificity and 96.5 % specificity [14]. The main drawbacks of these devices are sparse tissue sampling and their inability to assess the extent of the detected anomaly.

Imaging techniques offer a way to overcome sparse tissue sampling and fully visualize the extent of the disease. For example, optical imaging has shown excellent sensitivity towards differentiation of cancerous and healthy tissue [15–17]. However, purely optical imaging techniques struggle beyond ~1–2 mm [18–21]. Photoacoustic imaging (PAI), which has also shown promise at differentiating cancerous and healthy tissue [22,23], utilizes ultrasonic detection and can provide greater imaging depth compared to purely optical imaging techniques. Several groups have evaluated tomographic PAI for breast cancer margin assessment on excised specimens and have shown sensitivity and specificity comparable to intracavity RF and mass spectroscopy devices [24–26]. Furthermore, tomographic PAI is able to image the entire specimen, thereby overcoming sparse sampling and fully visualising the extent of the disease [17,27,28].

In PAI studies by Kosik et. al. [17,28] and Li et al. [24], lipid optical absorption was used to differentiate tumour tissue from healthy tissue [17,27,28]. Tumour tissue tended to have a lower lipid content compared to healthy tissue and as a result appeared dark (hypo-intense) in the images, whereas healthy tissue appeared bright (hyper-intense) [29]. Moreover, excised specimens typically have low haemoglobin content [28]. Therefore, the photoacoustic signal at 930 nm from lipids was expected to be the dominant contribution compared to haemoglobin. Kosik et al. (2022) also showed that hypo-intense regions in the PA images of lumpectomy specimens corresponded to the size of the tumour detected preoperatively with MRI [17].

PAI has yet to be tested in a real-time intracavity scenario during BCS. From a practical standpoint, hand-held PAI devices typically suffer from incomplete data collection caused by limited-view angle coverage. In addition, limitations posed by the limited frequency bandwidth of the acoustic sensor become more dominant in a hand-held scanning approach. These problems result in image artifacts, such as blurring, streaking and incomplete visualisation of objects [30–32]. Therefore, the main objective of this work was to determine the feasibility of a compact hand-held PAI probe designed specifically for breast cancer margin imaging based on the lipid content differences, as previously reported by Kosik et.al (2022).

In comparison to other hand-held PAI probes, this probe was designed with an increased sensitivity towards bulk tissue and with consideration towards the ultimate aim of free-hand scanning utilising a motion tracking system [33–37]. Typically, hand-held probes used in PAI have centre frequencies ranging from 5 to 21 MHz [33–35,37]. This results in visualisation of tissue constituents in the range of 0.07–0.3 mm and is ideal for imaging of vascular networks, but not optimal for imaging bulk tissue properties. When looking for differences in tissue constituents, such as lipid content, the bulk tissue properties are of increased interest. In terms of breast conserving surgery, the ability to confirm that the top layer of tissue mostly consists of healthy lipids can provide the surgeon with an estimate of the current margin status.

In this study, we present the design of a hand-held PAI probe

prototype and its imaging capabilities. The effect of limited-frequency bandwidth was investigated by conducting simulations and comparing to experimental results. The ability to visualise objects with hypo-intense contrast was assessed by imaging tissue mimicking phantoms consisting of regions with high and low optical absorption. The feasibility of the single-sensor imaging concept and the effect of limited-view was assessed by comparing imaging results of a breast cancer specimen phantom obtained with the prototype to an image acquired with a near full-view tomographic PAI system. Lastly, as a proof-of-concept, preliminary imaging of a lumpectomy specimen was performed.

2. Materials and methods

This section includes the methodology for a series of experiments conducted for the purpose of investigating the feasibility of the hand-held imaging approach. Preliminary work aimed towards characterisation of the hand-held PAI probe is included in the Supplementary data. For information on the illumination profile, sensor spatial sensitivity, frequency response and resolution please consult the Supplementary data.

2.1. Hand-held PAI probe design and characterisation

The prototype hand-held PAI probe was designed to provide both optical illumination and photoacoustic signal detection in the same instrument (Fig. 1a). An overview of the complete PA imaging system is shown in Fig. 1b. Illumination was provided by a 10-Hz Nd:YAG laser (Brilliant, Quantel, Bozeman, MT, USA) coupled to an optical parametric oscillator for wavelength tuning (Phocus™, Opotek Inc., Carlsbad, CA, USA). Short laser pulses (15 mJ, 5 ns) were delivered to a 1-to-4 optical fibre bundle (806–00006, Excelitas Canada Inc., Mississauga, ON, CA, NA 0.37). The output legs were positioned around the circumference of a cylindrical casing containing the acoustic sensor, an approach previously used by other groups [38,39]. Light from the fibre was focused with a polycarbonate axicon lens with a wall angle of 52°. In close proximity (0–15 mm) to the probe tip, the illumination profile consisted of four distinct bright spots which then converged, formed one uniform beam from 15 to 25 mm (see Suppl. Data.). Maximum light was delivered to the object at a probe to surface separation of 20–25 mm (focal depth). All imaging experiments were performed at this probe to surface separation. The illumination approach was similar to illumination methodologies used in photoacoustic microscopy [40].

The PA detection unit incorporated a circular (Ø13-mm) 500-μm-thick polyvinylidene difluoride (PVDF) piezoelectric element (Airmar Technology Corporation, Milford, NH, USA). The centre frequency of the acoustic sensor was 322 kHz with a bandwidth of 81 % at − 3 dB (see Suppl. data), which corresponded to a peak sensitivity to objects between 3.15 mm and 6.94 mm in size. The angular acceptance of the probe was estimated to be ~ 5°. The combined effect of the illumination profile and directionality of the acoustic sensor at a distance of 25 mm from the probe tip yielded a circular sensitivity region of 15 mm. The acoustic sensor, optical fibres and light guide were held together by two 3D printed parts and two optical rods.

Signals were digitized using a 14-bit, 50-MHz data acquisition system (DAQ32, MultiMagnetics Inc., London, ON, Canada) triggered by the laser. A photodiode (DET10A, Thorlabs Inc., Newton, NJ, USA) positioned behind a mirror in the light path recorded relative laser power measurements for each pulse. Pulse-to-pulse laser output energy variation was accounted for by dividing each PA signal by the corresponding laser power measurement.

2.2. Imaging experiments

Real-time data reconstruction and motion tracking were not feasible for the first prototype. Therefore, the location of the probe was controlled by mounting the probe to an industrial 6-axis robot (C3-
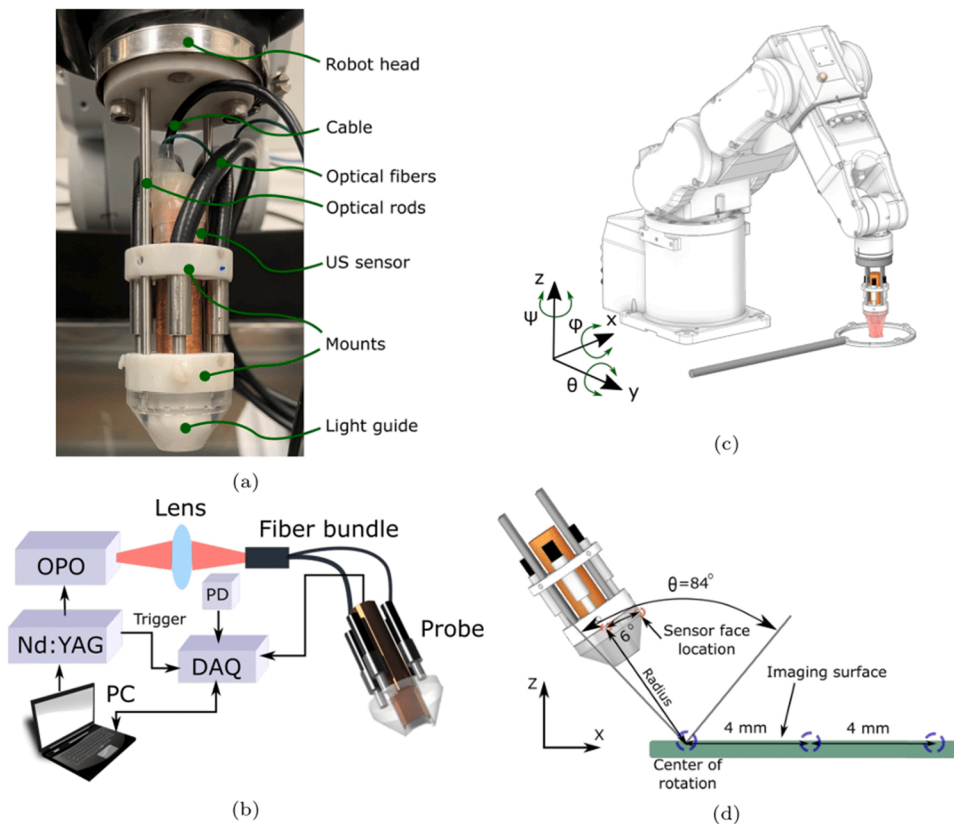
Fig. 1. (a) Photograph of the prototype hand-held PAI probe attached to a robot. The acoustic sensor casing, light guide and optical fibres were held together with two optical rods (Ø 4 mm) and two 3D printed mounts to align the sensor, optical fibres, and lens. (b) block diagram of the full imaging set up (robot not included in the diagram). The 4-to-1 optical fibre from the probe is coupled through a lens to the output of the optical parametric oscillator (OPO) attached to the 10 Hz Nd:YAG laser. Photodiode (PD) is positioned adjacent to the laser path to capture laser energy fluctuations. Data acquisition is started by software that saves the digitized data acquired by the data acquisition system (DAQ) and stores it into computers (PC) memory. The DAQ is triggered by the laser. (c) Illustration of the prototype hand-held PAI probe mounted on a robot with coordinate system and direction of rotation indications. (c) Illustration explaining scan geometry carried out with the probe attached to the robot end effector. All imaging experiments reported in this paper used this scan type. Probe is positioned a set distance from the imaging surface (Radius), typically 15–25 mm. Probe rotates over 84° in 6° increments in θ over each translational point with centre of rotation being the surface of the object being imaged. Red circles in the illustration are examples of sensor face location during angular steps, while the blue circles indicate the translational steps. Each translational step becomes a centre of rotation. The distance over which the probe was translated was dependant on the size of the object.

A601S-UL, Epson, Suwa, Japan) (Fig. 1c). For acoustic coupling, all experiments were performed in a water tank. All imaging with the hand-held probe was performed using the scan procedure depicted in Fig. 1d. The probe was translated in the x-direction in 4-mm increments (blue circles, Fig. 1d) and rotated around each translational step in θ over 84° in 6° increments (red circles, Fig. 1d). The distance over which the probe was translated depended on the size of the object. Scan of an 80 mm long object took approximately 1 min. Spatial sampling at increments smaller than 4-mm resulted in minor improvements in image quality (see Suppl. data). The scan resulted in an axial resolution of 1.0 mm and a lateral resolution of 1.8 mm (see Suppl. data). The scanning approach yielded angular coverage similar to what is expected to be possible inside a surgical cavity. Rotation of the probe about the φ axis was not possible due to limitations related to the water tank size and the robot reach.

The images were reconstructed with a delay and sum algorithm [41] including directivity weighting [42] using an open-source PAI reconstruction software package [43]. The collection of sensor positions was treated as an array for reconstruction purposes. The pixel size in all images was 0.02 mm. Forced zeroing was applied as the only post-processing step, unless otherwise stated [30].

2.3. Effect of limited frequency bandwidth

The effect of acoustic sensor frequency response on image quality was assessed with simulations and through an imaging experiment on two phantoms with lipid inclusions. To fabricate the phantoms, a rectangular mould (40 mm × 40 mm × 30 mm) was used. A 8 – 10 mm thick layer of 2 % w/v agarose (VWR Life Science Agarose RA™, Mississauga, ON, CA) and 4 % v/v Intralipid® (Fresenius Kabi Canada Ltd., Toronto, ON, CA) was poured into the mould to create a first layer ($\mu'_s = 1$ mm^{-1}). Once set, the fat inclusion was placed on top of the first layer

and the mould was backfilled with the agarose and intralipid mixture to envelope the inclusion. The fat was obtained from a piece of pork belly purchased at the local grocery store. The first phantom had a 9-mm thick fat layer with a 2.5-mm deep hole with a diameter of 9 mm. The second phantom had a 2-mm thick fat layer with a centrally located 5-mm through-hole.

The phantoms were placed in a water tank and imaged at 930 nm. This wavelength was selected as it corresponds to a spectral peak in lipid absorption [44]. While the lipid peak at 1200 nm is potentially more favourable, as absorption by other dominant chromophores and constituents such as water and haemoglobin is lower, we were limited to lasers available to us with a maximum achievable wavelength of 950 nm.

After imaging, the phantoms were cut along the scan line and the cross-sectional view was photographed. The lipid-containing portion of each phantom in each photograph was segmented and binarized to obtain a mask. The masks were used as initial pressure conditions for k-Wave simulations in MATLAB [45,46]. The photoacoustic signal from the mask was simulated using the same sensor locations used to image the phantoms. Two simulations were performed. The first simulation assumed unlimited bandwidth of the acoustic sensor. The second simulation assumed a centre frequency of 322 kHz with a bandwidth of 81 % for the acoustic sensor, to mimic the response of the acoustic sensor in the hand-held PAI probe. The speed of sound was set to 1500 m/s. In preliminary reconstructions, we investigated the effects of the speed of sound on the image quality in the range of 1450–1540 m/s but did not note any visible differences due to the small probe to image surface separation. The grid size was 36.4 mm by 20.4 mm with a pixel size of 0.02 mm. Uniform light propagation was assumed in the simulations; however, illumination was from one side during experiments. Comparison between experimental and simulated data suggested that the

uniform laser fluence assumption was reasonable since the main image degrading effects were related to US detection (i.e. sensor bandwidth and number of angular views). No post-processing was applied to the data.

2.4. Detection study

Three absorbing phantoms with eight non-absorbing rectangular slits (widths of 0.5, 1, 2, 3, 4, 5, 6, 7 mm) were made to validate the accuracy of hypo-intense object identification with the hand-held PAI probe. Each phantom had a set slit depth (2, 4 or 6 mm). The absorbing background consisted of 0.15 % v/v India ink (Speedball, Statesville, NC, USA), 2 % w/v agarose and 2 % v/v Intralipid®, resulting in μ_a= 0.54 mm^{-1} and μ_s'= 0.5 mm^{-1}. The slits were filled with 2 % w/v agarose and 2 % v/v Intralipid®. Each phantom was imaged with the hand-held PAI probe at 800 nm. The width of each slit was measured from the FWHM of the intensity line profile extracted in the lateral image direction. Slit depth was measured from the intensity line profile extracted in the axial image direction. The measured values were then compared to the expected distances.

2.5. Effect of limited-view angle coverage

The effect of limited-view on image quality was assessed by imaging a phantom mimicking an *ex-vivo* breast cancer specimen with both the hand-held PAI probe and a tomographic imaging system with near full-view data capture capabilities. The phantom was made of a chicken breast wrapped in a 2-mm thick layer of pork belly fat, both purchased at a local grocery store. The chicken simulated cancerous tissue with lower lipid content compared to the pork belly fat layer that simulated healthy tissue. A gap in the pork belly layer exposed the chicken breast to simulate a positive margin. The phantom was affixed as described by I. Kosik et al. [28] for breast cancer specimen imaging [28]. In brief, the phantom was placed in a resealable bag filled with saline. The bag was positioned on an inclined surface to push out most of the saline along with any air bubbles and then sealed. Multiple dots were placed on the bag using a permanent black marker as landmarks for image registration. Clear packing tape was used to create tabs on two sides of the bag, which were then punched to create four holes. Using the holes, the bag was attached to four posts mounted on a circular holder.

The phantom was imaged with the hand-held PAI probe, then flipped 180° to acquire information from the opposite side. Next, the phantom was imaged using a near full view photoacoustic tomography (PAT) system, reported elsewhere [47]. Briefly, the near full view system was comprised of eight illumination fibres and 64 PVDF-based unfocused detectors (circular apertures of 12.7 mm) divided into 16 modules (Superior Assemblies, Mississauga, ON, CA). Each module had two lower frequency, 0.4-MHz peak frequency (160 % bandwidth at −6 dB), and two higher frequency elements, 0.9-MHz peak frequency (185 % bandwidth at −6 dB). Detector modules and illumination fibres were evenly mounted around and oriented towards the centre of a circular ring mounted to the beforehand mentioned robot. Data acquisition and laser coupling followed the same protocol as reported above for the hand-held PAI probe. The array was raster scanned and rotated in Φ and θ to image the entire phantom. The near full-view system had an effective ~3.8π steradian spherical coverage and was designed for high sensitivity towards bulk tissue absorption with a spatial resolution of 0.7–2.0 mm. The 930-nm laser light was used in both imaging setups. Although the illumination profile for both imaging system was considerably different, comparison between both systems was considered valid due to the image quality being mainly determined by the US detection side rather than illumination. Images acquired from both sides of the phantom using the hand-held PAI probe were stitched together in ImageJ with the help of markers placed as landmarks [48]. The corresponding slice in the 3D image obtained with the tomographic system was found using 2D to 3D image registration in 3D Slicer with the

marker dots as landmarks [49].

2.6. Imaging of ex-vivo breast cancer specimen

As a proof of concept, a lumpectomy specimen was imaged using the hand-held PAI prototype. A patient diagnosed with early breast cancer and scheduled to undergo breast conversing surgery was asked to participate in the study. The study was carried out with informed consent as well as the approval of the institutional review board of The University of Western Ontario (UWO Research Ethics Board # 105467; Lawson Approval #R-14–311). After excision, specimen preparation followed the same procedure as described in the section above and elsewhere [28], except for a different resealable bag (S-1692, Uline, 3″x3″). It was confirmed that the bag material did not create significant photoacoustic signal by studying photoacoustic images of a bag filled with saline only. The bag was marked with black marker on two sides, serving as fiducials for image registration. Imaging of the specimen was performed in the same manner as described in the section above. Imaging did not interfere with the standard of care surgical procedure. In addition to the PA images, 2D X-ray projections were obtained with a Faxitron™ (OR v2.0 MDS2, Tucson, AZ, USA) as part of the standard of care.

3. Results

3.1. Effect of limited frequency bandwidth

The effect of limited detection bandwidth (band-limited) on image quality was investigated using two lipid phantoms (Fig. 2). The first phantom (Phantom 1) had a large fat void whereas the second phantom (Phantom 2) had a smaller fat void. Photographs of the phantoms are shown in Fig. 2a and b. The binary masks used to generate the initial pressure distribution for each photoacoustic imaging simulation are shown in Fig. 2c. The time series simulated from each initial pressure distribution was then reconstructed into a photoacoustic image for the wide-band (Fig. 2d) and band-limited cases (Fig. 2e).

Reconstructions using the simulated wide-band data closely reproduced the shape of each lipid inclusion. The edges and crevasses of the reconstructed lipid inclusion were sharply defined. However, negativity artifact appearing as shadowing was observed at the bottom of each reconstructed lipid inclusion (Fig. 2d, white arrows). Reconstructions that utilized the simulated limited-band data had less-defined edges with negativity artifacts at the lipid inclusion boundaries (Fig. 2e, yellow arrows). However, regions without lipid, such as the crevasse in phantom 1 and the through hole in phantom 2 were easily identified (Fig. 2e). Furthermore, within the lipid regions, the bulk lipid signal was not observable in the limited-band reconstructions as compared to the wide-band reconstructions.

When comparing the experimental results to the simulated results, negativity artifacts similar to those present in the simulated limited-band data were observed (Fig. 2f, yellow arrows). In addition, the lipid distributions within each phantom were less-defined compared to the wide-band simulated data (c.f. Fig. 2d). However, the regions lacking lipids were easily identified for both phantoms. One of the major differences between the experimental and simulated results was the poor reconstruction of the bottom portion of phantom 1 due to insufficient light penetration and illumination provided only from one side of the phantom (Fig. 2f, top panel).

3.2. Detection study

Ability to detect hypo-intense contrast was investigated using slit phantoms with a series of hypo-intense features. The width and depth of the slits were measured from PA images and compared to the known slit dimensions. A photograph of a cross-section through the slit phantom with a slit depth of 6 mm is presented in Fig. 3a. Photographs of the
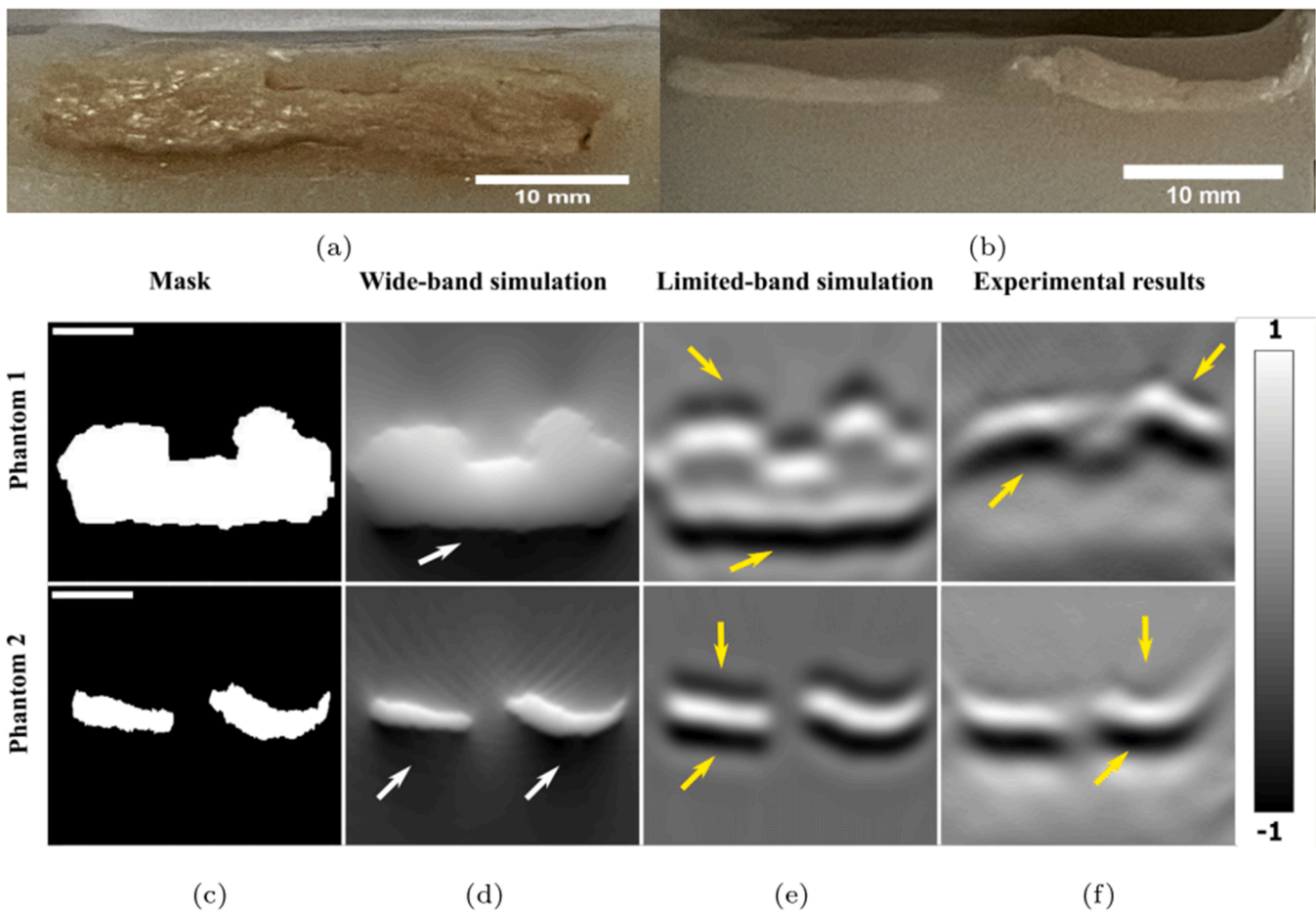
Fig. 2. Lipid phantom imaging and simulation study results. The scale bars correspond to 10 mm in all images. Photograph of (a) phantom 1 and (b) phantom 2 with ~ 8.7 mm and ~2 mm thick lipid inclusions, respectively. (c) Masks used as the initial pressure distribution for photoacoustic simulation of the phantoms in photographs (a) and (b), respectively. (d) and (e) Reconstructed PA images from simulated time series data with wide-band and limited-band (centre frequency of 322 kHz, bandwidth of 81 %) frequency response, respectively. White arrows and yellow arrows indicate negativity artifacts. (f) Photoacoustic images obtained with the hand-held probe of the phantoms in photographs (a) and (b). Scale bar on right side is common to all reconstructed images presented. For the binary mask image, black corresponds to 0.

remaining slit phantoms are available in the supplemental materials.

The PA images of the slit phantoms with 2 mm, 4 mm, and 6 mm slit depth are presented in Fig. 3b-d, respectively. Slit features, such as the sides and bottom of slits down to 2 mm in width can be clearly visualised in the PA images for all three phantoms. Slits with widths of 1 and 0.5 mm can be identified, but not clearly distinguished from the background material due to blurring. In all images, only the top portion (~ 4 mm) of each phantom was visualised. The bottom of each slit was clearly visualized for the six largest slit widths in each of the phantoms. However, image contrast degraded as the slit depths increased. For the six largest slits, the average difference between the measured and expected slit depth was 0.31 mm ± 0.48 mm.

The slit width for each phantom was measured by finding the FHWM in the lateral cross-sectional intensity plots (Fig. 3e). Each drop in intensity indicated the presence of a hypo-intense feature (i.e., slit). The slit width and depth were measured for each image and plotted against the expected values (Fig. 3 f) from the phantom mould. The average deviation from the expected slit width was 1.36 mm. The deviation from the expected slit width along with the standard deviation increased as slit width decreased. For a slit width of 7 mm, the average deviation from the expected value was 0.45 ± 0.10 mm and increased to 2.93 ± 0.46 mm for a slit width of 0.5 mm.

3.3. Effect of limited-view angle coverage

A breast cancer lumpectomy specimen phantom was imaged with the hand-held PAI probe to evaluate its feasibility for ex-vivo specimen imaging. In addition, the results were compared to PA images of the same phantom using a near full-view PAT system to evaluate the effect of limited-view angle coverage. Photographs of the top and bottom of the lumpectomy phantom are shown in Fig. 4a and b, respectively. The phantom was constructed with a simulated positive margin on the top surface (arrow in Fig. 4a). Lipid containing phantom regions produced strong photoacoustic signals (a RF data example is shown in Fig. 4c). However, the signal peak was surrounded by a negative signal (see item 1 in Fig. 4c) resulting from the limited angular view. To make image interpretation easier forced zeroing was utilized for image display. Furthermore, it can be seen that there was a secondary peak following the signal peak (see item 2 in Fig. 4c), which corresponded to a ghost artifact due to ringing of the sensor. Two-dimensional PA images of both the top (Fig. 4d) and the bottom (Fig. 4e) of the phantom were acquired with the hand-held PAI probe. The latter was acquired after rotating the phantom 180° about the *y*-axis. Image artifacts were noticeable as a ghost image offset in the *z*-direction (Fig. 4d, red arrow). The two PA images acquired with the hand-held probe were superimposed using fiducial markers on the specimen holder (Fig. 4d, c, green arrows) to visualise the entire cross-section of the phantom (Fig. 4f). Aside from the ghost artifacts, the signal in the image was confined to the lipid layer
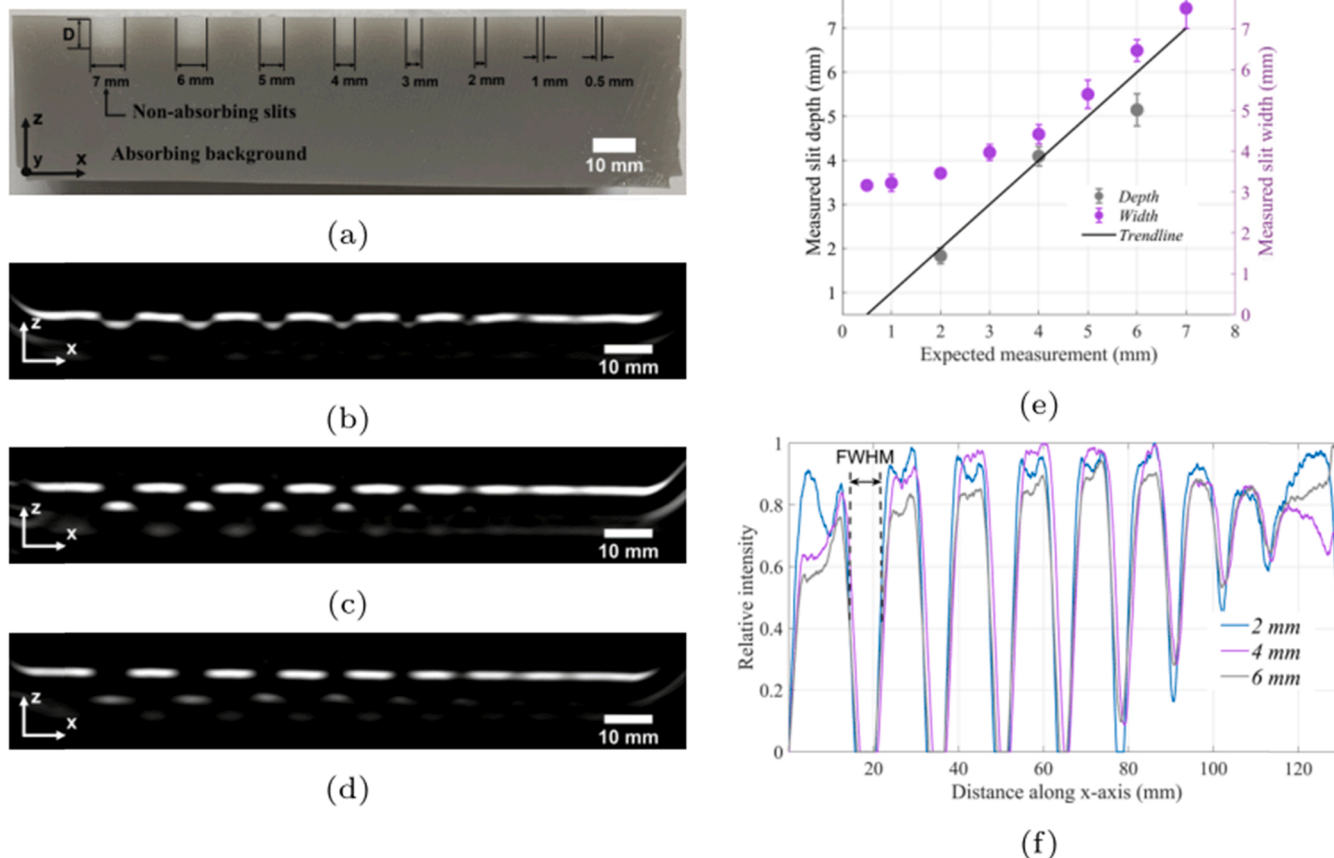
Fig. 3. Hypo-intense contrast detection study results. (a) Photograph of the slit phantom with 6-mm slit depth (D) with indication of phantom design details and slit widths. (b-d) Photoacoustic images of slit phantoms obtained with the hand-held PAI probe with slit depths (D) of 2, 4, and 6 mm, respectively. (e) Measured mean slit width and slit depth for all three phantoms plotted against the expected (known) measurement. Error bars represent ± 1 standard deviation of the mean. (f) Line profiles extracted from the PA images of the phantoms with slit depths of 2-, 4- and 6-mm. Panel indicates an example of a FWHM determination.

representing a layer of healthy breast tissue. The chicken breast (mimicking breast cancer tissue) 'positive margin' was clearly detected as a lack of signal in the middle portion and on the surface of the phantom (Fig. 4f, yellow arrow).

The phantom was also imaged with the near full-view PAT system and a *yz*-slice corresponding to the hand-held images was extracted from the 3D data volume (Fig. 4 g). Similar to the images obtained with the hand-held PAI probe, signal was confined to the lipid layer surrounding the mimicked breast cancer tissue and fiducial markers on the specimen holder (Fig. 4 g, green arrow). The mimicked positive margin was also detected (Fig. 4 g, yellow arrow); however, it was not as distinct and blurred compared to images obtained with the hand-held PAI probe (compare Fig. 4 f and g). Differences in the signal-to-noise levels between the hand-held PAI probe and the near-full view system can be well visualized in Fig. 4c.

The images from the two systems were then displayed as a false-colour overlay for comparison (Fig. 4 h). Based on the overlay, the image captured with the near full-view PAT system was blurred and had lower signal-to-noise compared to the images captured with the hand-held PAI probe. However, the images obtained with the hand-held probe had signal dropouts on the left and right side of the phantom and suffered from a greater number of image artifacts. The image overlay revealed close correspondence between the two PAI systems in terms of shape, and presence of the simulated positive margin on the lumpectomy phantom. A noticeable difference between the two images is the apparent thickness of the fat layer. The thickness of the fat layer in the images obtained with the hand-held probe is uniform, while in image from the near full-view PAT system thickness varies. This indicates that

hand-held PAI probe is suitable for imaging of only the very surface as it is not capable to recover the correct thickness of the layer.

3.4. Imaging of ex-vivo breast cancer specimen

A breast cancer lumpectomy specimen was imaged with the hand-held PAI probe to evaluate feasibility for ex-vivo specimen imaging. Photographs of the top and bottom of the lumpectomy specimen are shown in Fig. 5a and b, respectively. A two-dimensional X-ray image of the specimen was acquired with the same orientation as Fig. 5a as a part of the standard of care procedure (Fig. 5c). Two-dimensional PA images of both the top (Fig. 5d) and the bottom (Fig. 5e) of the specimen were acquired with the hand-held PAI probe. The latter was acquired after rotating the specimen 180° about the *y*-axis. The top and bottom images were registered using black marker lines as landmarks (Fig. 5d and e, green arrows) and superimposed to obtain a complete view of the specimen cross section (Fig. 5f).

Negativity artifacts were noticeable as shadowing beneath positive signal relative to the surface of the specimen, similar to artifacts seen in the results shown in Fig. 4. Signal from a surgical suture placed on the specimen surface by the surgeon for orientation purposes was a dominant feature in the PA image (Fig. 5 f, yellow arrow). As a result, signal from the surface of the specimen had lower SNR compared to the sutures and the phantom experiment reported in the previous section (Fig. 4). Forced zeroing removed the negative signal seen in (Fig. 5d-f), but enhanced visibility of the ringing artifacts (Fig. 5 g, blue arrow).
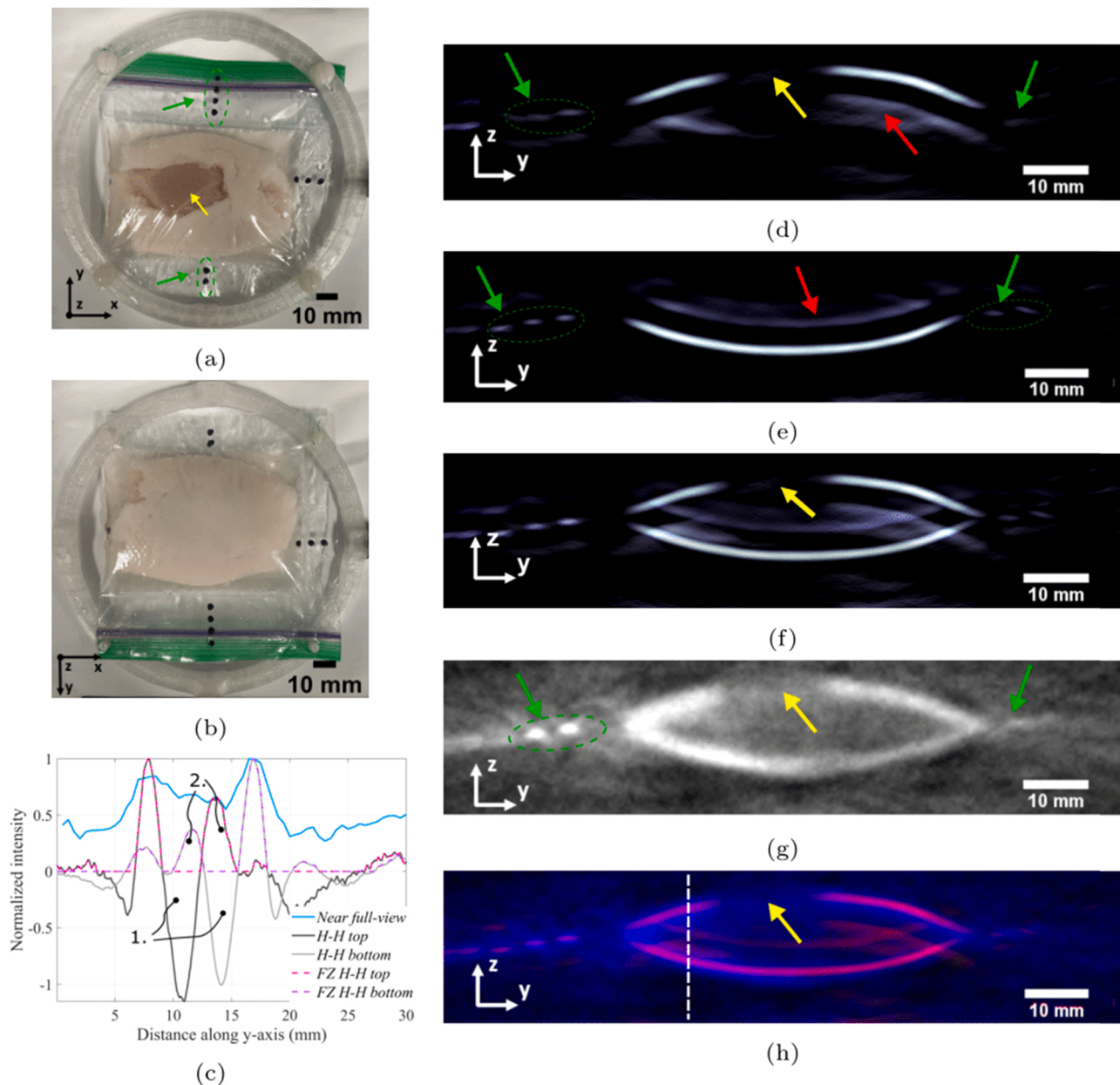
Fig. 4. Comparison of PA images of a lumpectomy phantom acquired with the hand-held PAI probe and a near full-view PAI system. (a) A photograph of the top and (b) bottom portion of the lumpectomy phantom. (c) radio-frequency (RF) data of the images presented in (d) FZ H-H top, (e) FZ H-H bottom and (g) near full-view through the cross section of the phantom as indicated by white dashed line in (h). RF data of raw photoacoustic signal from the hand-held probe is also presented (H-H top and H-H bottom). Please note that RF signal is presented in a way it appears in the overlayed image, meaning signal obtained with the hand-held PAI probe from the bottom lipid layer is inverted. The signal peak corresponds to the signal from the lipid-layer. It is preceded and followed by a negative signal (1.). The second peak following the highest peak (2.) was likely due to ringing of the sensor. (d) Forced zeroed PA image of the top and (e) bottom surface of lumpectomy phantom acquired with the hand-held PAI probe with indication of fiducial markers (green arrow) and artifacts (red arrow). (f) Overlay of the PA images of the top and bottom surfaces of the lumpectomy phantom corresponding to (d) and (e), respectively. (g) PA image of the lumpectomy phantom acquired with a near full-view PAT system. (h) Overlay of images shown in panels (f) and (g), with colour coding in pink and blue, respectively. The yellow arrows indicate the location of the mimicked positive margin. The green arrows indicate the fiducial markers from the phantom holder.

4. Discussion

We have developed a prototype hand-held PAI probe intended for breast cancer margin assessment based on lipid content differences. The probe provided optical illumination and acoustic detection in a single instrument and enabled imaging of the surface of an excised lumpectomy specimen and potentially the wall of the surgical cavity. Additionally, while cancer detection based on lipid content differences has been suggested before, it has never been tested with in a single-sensor design optimized for low frequency detection of bulk tissue properties.

In this work, we demonstrated the feasibility of this concept by examining the effects of limited view angle and limited frequency bandwidth posed by a hand-held device.

Experiments with the prototype hand-held PAI probe at 930 nm resulted in excellent image contrast from lipids (e.g. see Fig. 4). Lipid free gaps mimicking positive margins were clearly visible in the images. Breast cancer on average contains 6 times less lipid compared to healthy tissue [50]. Our tissue phantom was comprised of chicken breast, which on average contained 14 % fat. The phantom also contained pork belly fat, which was 7 times fattier than chicken breast thereby providing a
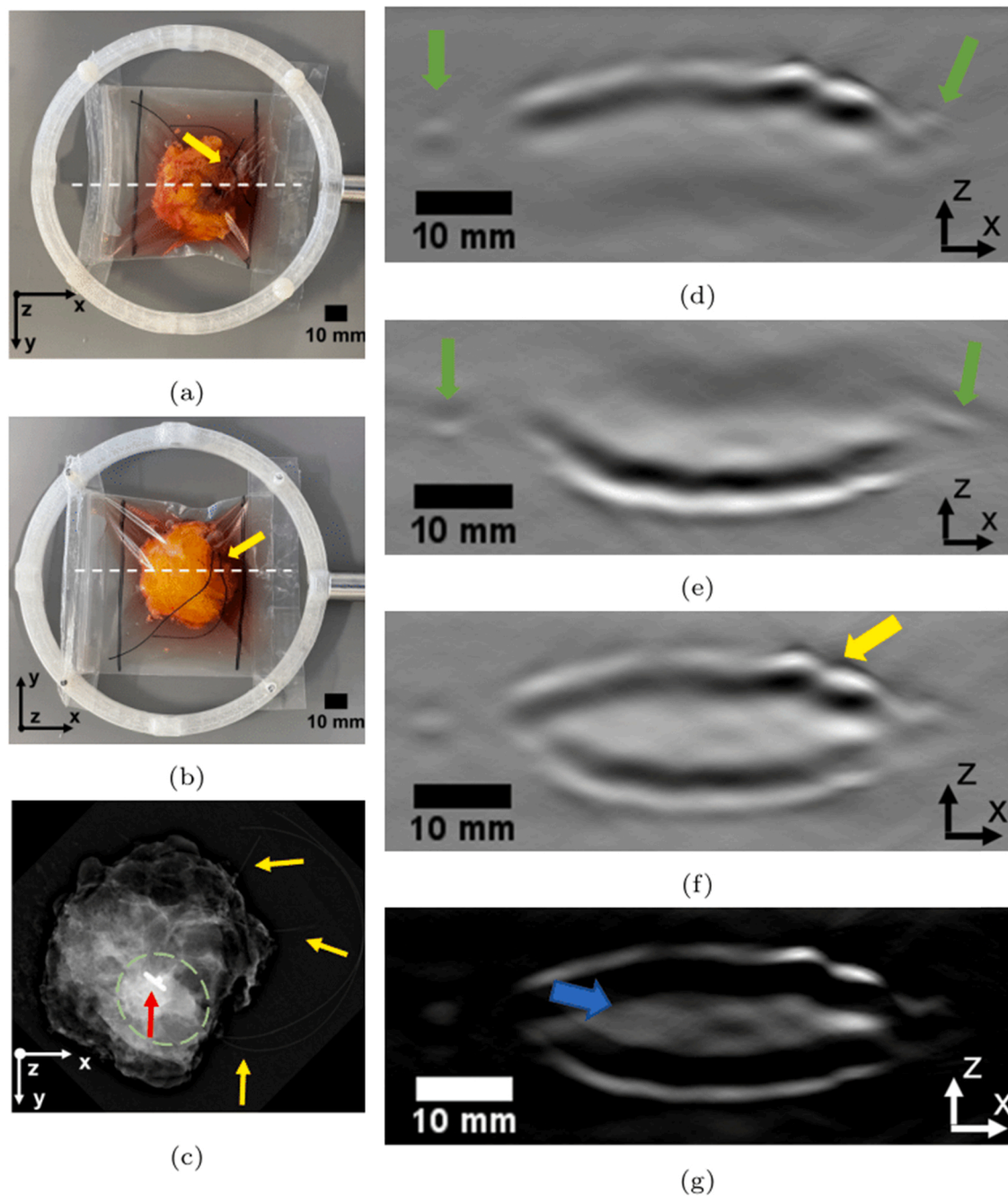
Fig. 5. Lumpectomy specimen imaging results. (a) A photograph of the top and (b) bottom of the lumpectomy specimen placed in a bag with black fiducial markers and secured on a holder. Yellow arrows indicate the location of the surgical sutures. (c) 2D X-ray image of the lumpectomy specimen (scale unknown) with similar orientation to panel (a). Red arrow indicates location of the radioactive seed. Location of the cancerous tissue is indicated with a dashed circle. (d) Raw PA image of the top and (e) bottom surface of lumpectomy specimen acquired with the hand-held PAI probe with indication of fiducial markers (green arrows). The white dashed line in images (a) and (b) represent imaging plane for images (e) and (d), respectively. (f) Registered and superimposed PA image of the top and bottom of the lumpectomy specimen corresponding to (e) and (f), respectively. Signal from the surgical sutures is indicated with yellow arrows. (g) Forced zero PA image of the lumpectomy specimen. The blue arrow indicates the location of the ringing artifacts.

good approximation of the photoacoustic contrast differences between cancerous and healthy tissue. The lack of contrast between the coupling medium and the lipid-free gaps (i.e., the specimen surface) presented a challenge for the 930 nm imaging approach. However, multi-wavelength PAI and/or incorporation of pulse/receive ultrasound imaging into the probe could be used to detect the specimen surface.

The prototype hand-held PAI probe allowed for the identification of hypo-intense features with characteristic dimensions of 0.5–7.0 mm in width and 2–6 mm in depth. This provided an indication that the probe could potentially identify residual cancerous tissue, represented as lack of signal, extending up to 6 mm into the surgical cavity wall or into an excised specimen. In addition, signal obtained from the absorbing background of the slit phantom showed that full visualisation of hyper-intense features was possible up to 5.3 mm in depth. This indicated that a margin of healthy tissue can potentially be visualized up to this depth. It needs to be pointed out that the geometry of the slit phantom might have improved the image quality compared to what would be achievable in a surgical scenario. The slits in the phantom were extended in length

in the out of plane dimension. This was a consequence of the fabrication procedure. Given that the sensor response and illumination was highly directional (see Fig. 3 in Supplementary data), we expected the contribution of out plane signal to be negligible, however, a rectangular feature will emit a substantially planar wave that will reach different parts of sensor simultaneously possibly leading to improved image quality. However, this situation could also be encountered in some surgical scenarios.

The lumpectomy specimen imaging study showed (Fig. 5) that a strong signal can be obtained from fatty tissue. Contrast appeared lower compared to the images obtained in the phantom imaging study (Fig. 4). The optical absorption and, therefore, the photoacoustic signal from the surgical sutures were a few orders of magnitude higher than the signal from fatty tissue. The presence of the sutures made signals from the surface of the specimen appear visually weaker in the reconstructed images. This issue will not affect intracavity imaging due to the absence of sutures. Also, specimen imaging with the probe in a free-hand mode will give the operator the opportunity to avoid sutures during imaging tasks. Moreover, in the future, multispectral photoacoustic imaging could aid in differentiation of the sutures from tissue. One interesting finding from the lumpectomy study related to the delineation of the specimen surface. The reconstructed surface, although well delineated, had a much smaller thickness than expected on account of fatty tissue throughout the specimen. The finding indicated that the width of the surface feature may not be indicative of the thickness of the fatty tissue. Although the reason for this effect is unknown, it is likely related to a variety of factors such as limited light penetration depth, narrow frequency response of the sensor, and limited angular views used to reconstruct the image. The finding suggests that the identification of close margins might not be possible with this imaging approach. However, the probe is likely to be a valuable tool for identification of positive margins at the surface of the specimen or surgical cavity.

A major limitation of the hand-held PAI probe related to the presence of negativity artifacts in the PA images. Negativity artifacts arose from limited bandwidth and limited view angle of the detector as described elsewhere [30]. Detector bandwidth can potentially be improved with different piezoelectric materials; however, the range of detector view angles is limited by the maximum achievable angle between the probe and the cavity wall. In our simulations, we used an angular range of $\pm 42°$ and both flat and limited frequency response. Image reconstruction with simulated wide-band data resulted in negativity artifacts that appeared as minor shadowing and did not notably alter the image quality. In contrast, image reconstruction with experimentally collected data and simulated limited bandwidth data had notably larger negativity artifacts appearing as signal dropouts above and below the signal from the fat layer. Therefore, it can be concluded that the presence of negativity image artifacts in the experimental work was due primarily to the limited bandwidth of the sensor. Overall, the simulations and experimental results give confidence that angular coverage of $\pm 42°$ can provide sufficient image quality given a sensor with appropriate bandwidth. However, in situ experiments will ultimately determine if $\pm 42°$ is a practical angular range.

Comparison of imaging results from the hand-held PAI probe with the full-view PAI system revealed that negativity artifacts could also be reduced by having more angular views. Image quality was notably improved when the hand-held PAI probe was both translated and rotated through a greater number of angular views. However, rotation of the hand-held PAI probe was limited to a single dimension due to restrictions posed by the robot reach and the size of the water tank. A more compact probe will offer the possibility to study a greater range of angles and more complex scan arrangements.

The negativity artifacts present in images acquired with the hand-held PAI probe were unavoidable due to the limited bandwidth and limited view angle intrinsic to the design. However, we found that these artifacts could be mitigated by post-processing the images with forced zeroing as previously suggested by K. Shen et.al (2020). Forced zeroing

produced images that were easier to interpret due to the elimination of the negative signal. However, the introduction of forced zeroing comes with the cost of size overestimation of hypo-intense objects and underestimation of hyper-intense objects. Additionally, artifacts could potentially be mitigated by deconvolution of the acquired data with the impulse response of the sensor. This could also improve the visibility and detectability of objects outside of the -3 dB bandwidth range, as the sensor frequency response extends from 100 kHz to 2 MHz. Sensor material selection was mainly based on the stock availability from manufacturers. We aimed for optimization at lower frequencies which required thick PVDF film. Larger bandwidth and a higher centre frequency would likely yield better visualisation of the top 2 mm.

A solid sensor backing was incorporated into the probe, which reflected acoustic waves back into the sensor material. Although a solid backing degraded image resolution 2-fold due to the back-and-forth travel of acoustic waves though the sensor, it also resulted in an increase in detection sensitivity. However, the stiffness of the solid backing layer was not sufficient to dampen all sensor oscillations. The sensor oscillations resulted in ringing that generated ghosting artifacts in the reconstructed images. Typically, US sensors have an acoustically matched backing layer that guides the incoming acoustic wave away from the sensor element and dampens reverberations. However, sensitivity of a sensor with a matched backing layer is reduced compared to a sensor with a solid backing layer. Therefore, the trade-off between sensitivity and presence of artifacts needs to be examined closer. While artifacts degrade the image quality, lower sensitivity affects image quality also.

For the hand-held probe to be useful as a free-hand imaging instrument, the location and orientation of the probe relative to a reference point must be determined in real-time. Preliminary work with an electromagnetic tracking system (not shown) was largely unsuccessful. While other research groups have shown the ability to obtained accuracy up to 0.2 mm on average using electromagnetic tracking, we were not able to achieve such accuracy and precision due to sensitivity towards metal inside the probe and in nearby structures [51]. We, therefore, utilized a 6-axis robot to perform scanning procedures with the hand-held probe. The probe was scanned linearly and through a wide range of angles. This allowed to achieve a sub-millimetre accuracy and precise repeatability thereby ensuring reconstructed images were not affected by probe positioning errors both within an image and between images. In a surgical scenario, the probe will be moved freely inside the surgical cavity, which necessitates real-time positional tracking of the probe. We propose that a camera-based optical tracking method might be well-suited for this application. Depending on the achievable accuracy of the positional data obtained from the optical tracking, free-hand scanning can possibly allow for more angular positions (not only in θ, but also φ) reducing the impact of image artifacts.

Currently available hand-held tools for breast cancer margin assessment generally provide a binary output (yes/no) and tend to sparsely sample tissue without the ability to discriminate depth. Depth discrimination is important for correlating results to pathology in some cases (e.g. 2 mm DCIS criteria) [2]. For example, the MarginProbe® is able to provide information only up to 1 mm in depth, ClearEdge up to 3 mm, while iKnife removes a piece of tissue in the size range of $0.1–1\ mm^3$ from the point of interest on the surgical specimen [13,14, 52]. In comparison, the hand-held PAI probe provides a continuum of image contrast at useful depths from the surface, although optimisation is needed for human tissue. Furthermore, the probe enables dense sampling at fixed points or across a region of interest due to the high repetition rate of the pulsed laser (10 Hz). Additionally, compared to mass spectrometry techniques, it is non-destructive to tissue.

Future work on the hand-held PAI probe is needed in three areas. First, the probe needs to be miniaturised to fit inside the surgical cavity. Second, free-hand imaging with the probe needs to be demonstrated. The addition of optical positional tracking is likely to provide real-time data with the accuracy and precision needed to generate PA images with

free-hand scanning. This will allow the surgeon to advance the probe and build up an image of the region of interest in real-time. Third, the probe needs to be tested on excised breast cancer specimens as optical characteristics of phantoms are only representative of human tissue due to weak anisotropic scattering and do not fully simulate real tissue.

5. Conclusion

The feasibility of a hand-held PAI probe designed to detect cancerous tissue based on lipid content differences was assessed. The hand-held PAI probe was able to image hypo-intense contrast features in phantoms that were representative of a positive surgical margin and provided a strong signal from fatty tissue in a lumpectomy specimen. Detection of objects with hypo-intense contrast down to 0.5 mm in width and up to 6 mm in depth was achieved. However, the limited bandwidth of the sensor combined with the limited range of view-angles resulted in image artifacts. Nevertheless, images captured with the hand-held probe had higher contrast compared to images captured with a near full-view PAT system. Further work on probe miniaturisation and additional testing on human lumpectomy specimens is needed to ensure the technology is suitable for intra-operative margin assessment during breast conserving surgery.

Declaration of Competing Interest

The authors declare the following financial interests/personal relationships which may be considered as potential competing interests: Jeffrey Carson reports financial support was provided by FACIT. Jeffrey Carson reports a relationship with Multimagnetics Inc. that includes: equity or stocks and funding grants. Jeffrey Carson has patent #US9128032 pending to Multimagnetics Inc.

Acknowledgments

Appendix A. Supporting information

Supplementary data associated with this article can be found in the online version at doi:10.1016/j.pacs.2022.100424.

References

[1] J. Ellrant, E. Plassgård, P.-O. Bendahl, L. Rydén, Risk factors for reoperation following breast-conserving surgery integrated into pre- and postoperative models with high accuracy, in: Poster Sess. Abstr., American Association for Cancer Research, 2019: pp. P3–13-03-P3–13–03. https://doi.org/10.1158/1538–7445. SABCS18-P3–13-03.

[2] E.-E.S. Buchholz, T.A. Somerfield, M.R. Griggs JJ, Margins for breast-conserving surgery with whole-breast irradiation in stage I and II invasive breast cancer: American Society of Clinical Oncology endorsement of the Society of Surgical Oncology/American Society for Radiation Oncology consensus guideline, J. Clin. Oncol. 32 (2014) 1502–1506, https://doi.org/10.1200/JCO.2014.55.1572.

[3] M.S. Moran, S.J. Schnitt, A.E. Giuliano, J.R. Harris, S.A. Khan, J. Horton, S. Klimberg, M. Chavez-MacGregor, G. Freedman, N. Houssami, P.L. Johnson, M. Morrow, Society of surgical oncology–American Society for radiation oncology consensus guideline on margins for breast-conserving surgery with whole-breast irradiation in stages I and II invasive breast cancer, Int. J. Radiat. Oncol. 88 (2014) 553–564, https://doi.org/10.1016/j.ijrobp.2013.11.012.

[4] W.J. Gradishar, M.S. Moran, J. Abraham, R. Aft, D. Agnese, K.H. Allison, S.L. Blair, H.J. Burstein, C. Dang, A.D. Elias, S.H. Giordano, M.P. Goetz, L.J. Goldstein, S.

A. Hurvitz, S.J. Isakoff, R.C. Jankowitz, S.H. Javid, J. Krishnamurthy, M. Leitch, J. Lyons, J. Matro, I.A. Mayer, J. Mortimer, R.M. O'Regan, S.A. Patel, H. S. Rugo, A. Sitapati, K.L. Smith, M. Lou Smith, H. Soliman, E.M. Stringer-Reasor, M. L. Telli, J.H. Ward, K.B. Wisinski, J.S. Young, J.L. Burns, R. Kumar, NCCN Guidelines® insights: breast cancer, version 4.2021: featured updates to the NCCN Guidelines, J. Natl. Compr. Cancer Netw. 19 (2021) 484–493, https://doi.org/10.6004/JNCCN.2021.0023.

[5] S. Fisher, Y. Yasui, K. Dabbs, M. Winget, Re-excision and survival following breast conserving surgery in early stage breast cancer patients: a population-based study, BMC Health Serv. Res. 18 (2018) 94, https://doi.org/10.1186/s12913-018-2882-7.

[6] L. Care, K. Kaczmarski, P. Wang, R. Gilmore, H.N. Overton, D.M. Euhus, L. K. Jacobs, M. Habibi, M. Camp, M.J. Weiss, M.A. Makary, Surgeon re-excision rates after breast-conserving surgery: A Measure, e2, J. Am. Coll. Surg. 228 (2019) 504–512, https://doi.org/10.1016/j.jamcollsurg.2018.12.043.

[7] J.M. Jorns, D. Visscher, M. Sabel, T. Breslin, P. Healy, S. Daignaut, J.L. Myers, A. J. Wu, Intraoperative frozen section analysis of margins in breast conserving surgery significantly decreases reoperative rates: one-year experience at an ambulatory surgical center, Am. J. Clin. Pathol. 138 (2012) 657–669, https://doi.org/10.1309/AJCP4IEMXCJ1GDTS.

[8] K. Esbona, Z. Li, L.G. Wilke, Intraoperative imprint cytology and frozen section pathology for margin assessment in breast conservation surgery: a systematic review, Ann. Surg. Oncol. 19 (2012) 3236–3245, https://doi.org/10.1245/s10434-012-2492-2.

[9] M.C. Kaufman, C.S. Jacobson, L. Bachman, B.A. Kaufman LB, Intraoperative digital specimen mammography: rapid, accurate results expedite surgery, Ann. Surg. Oncol. 14 (2007) 1478–1485, https://doi.org/10.1245/S10434-006-9126-5.

[10] W.R. Keller, M.D. Vargis, E. de Matos Granja N, Development of a spatially offset Raman spectroscopy probe for breast tumor surgical margin evaluation, J. Biomed. Opt. 16 (2011) 077006, https://doi.org/10.1117/1.3600708.

[11] B.W. Maloney, D.M. McClatchy, B.W. Pogue, K.D. Paulsen, W.A. Wells, R.J. Barth, Review of methods for intraoperative margin detection for breast conserving surgery, J. Biomed. Opt. 23 (2018) 1, https://doi.org/10.1117/1.JBO.23.10.100901.

[12] M. Thill, MarginProbe®: intraoperative margin assessment during breast conserving surgery by using radiofrequency spectroscopy, Http://Dx.Doi.Org/10.1586/Erd.13.5. 10 (2014) 301–315. https://doi.org/10.1586/ERD.13.5.

[13] J.M. Dixon, L. Renshaw, O. Young, D. Kulkarni, T. Saleem, M. Sarfaty, R. Sreenivasan, C. Kusnick, J. Thomas, L.J. Williams, Intra-operative assessment of excised breast tumour margins using ClearEdge imaging device, Eur. J. Surg. Oncol. 42 (2016) 1834–1840, https://doi.org/10.1016/J.EJSO.2016.07.141.

[14] J. Balog, L. Sasi-Szabó, J. Kinross, M.R. Lewis, L.J. Muirhead, K. Veselkov, R. Mirnezami, B. Dezso, L. Damjanovich, A. Darzi, J.K. Nicholson, Z. Takáts, Intraoperative tissue identification using rapid evaporative ionization mass spectrometry, Sci. Transl. Med. 5 (2013), https://doi.org/10.1126/scitranslmed.3005623.

[15] G. Quarto, L. Spinelli, A. Pifferi, A. Torricelli, R. Cubeddu, F. Abbate, N. Balestreri, S. Menna, E. Cassano, P. Taroni, Estimate of tissue composition in malignant and benign breast lesions by time-domain optical mammography, Biomed. Opt. Express 5 (2014) 3684, https://doi.org/10.1364/boe.5.003684.

[16] P. Taroni, A.M. Paganoni, F. Ieva, A. Pifferi, G. Quarto, F. Abbate, E. Cassano, R. Cubeddu, Non-invasive optical estimate of tissue composition to differentiate malignant from benign breast lesions: A pilot study, Nat. Publ. Gr. (2016), https://doi.org/10.1038/srep40683.

[17] I. Kosik, M. Brackstone, A. Kornecki, A. Chamson-Reig, P. Wong, J.J.L. Carson, Lipid-weighted intraoperative photoacoustic tomography of breast tumors: volumetric comparison to preoperative MRI, Photoacoustics 18 (2020), 100165, https://doi.org/10.1016/j.pacs.2020.100165.

[18] F.T. Nguyen, A.M. Zysk, E.J. Chaney, J.G. Kotynek, U.J. Oliphant, F.J. Bellafiore, K. M. Rowland, P.A. Johnson, S.A. Boppart, Intraoperative evaluation of breast tumor margins with optical coherence tomography, Cancer Res. 69 (2009) 8790, https://doi.org/10.1158/0008-5472.CAN-08-4340.

[19] A.S. Haka, Z. Volynskaya, J.A. Gardecki, J. Nazemi, J. Lyons, D. Hicks, M. Fitzmaurice, R.R. Dasari, J.P. Crowe, M.S. Feld, In vivo margin assessment during partial mastectomy breast surgery using raman spectroscopy, Cancer Res. 66 (2006) 3317–3322, https://doi.org/10.1158/0008-5472.CAN-05-2815.

[20] V. Krishnaswamy, A.M. Laughney, W.A. Wells, K.D. Paulsen, B.W. Pogue, Scanning in situ spectroscopy platform for imaging surgical breast tissue specimens, Opt. Express 21 (2013) 2185, https://doi.org/10.1364/OE.21.002185.

[21] T.M. Bydlon, S.A. Kennedy, L.M. Richards, J.Q. Brown, B. Yu, M.K. Junker, J. Gallagher, J. Geradts, L.G. Wilke, N. Ramanujam, Performance metrics of an optical spectral imaging system for intra-operative assessment of breast tumor margins, Opt. Express 18 (2010) 8058, https://doi.org/10.1364/OE.18.008058.

[22] K.S. Valluru, J.K. Willmann, Clinical photoacoustic imaging of cancer., Ultrason. (Seoul, Korea). 35 (2016) 267–80. https://doi.org/10.14366/usg.16035.

[23] K. Kincade, Optoacoustic Imaging/Photoacoustics: the wide-ranging benefit of photoacoustic commercialization, IEEE Pulse 6 (2016) 28–33, https://doi.org/10.1109/MPUL.2015.2409099.

[24] R. Li, P. Wang, L. Lan, F.P. Lloyd, C.J. Goergen, S. Chen, J.-X. Cheng, Assessing breast tumor margin by multispectral photoacoustic tomography, Biomed. Opt. Express 6 (2015) 1273, https://doi.org/10.1364/boe.6.001273.

[25] R. Li, L. Lan, Y. Xia, P. Wang, L.K. Han, G.L. Dunnington, S. Obeng-Gyasi, G. E. Sandusky, J.A. Medley, S.T. Crook, J.-X. Cheng, High-speed intraoperative assessment of breast tumor margins by multimodal ultrasound and photoacoustic tomography, Med. Devices Sens. 1 (2018), e10018, https://doi.org/10.1002/MDS3.10018.

[26] R. Zhang, L. Zhao, C. Zhao, M. Wang, S. Liu, J. Li, R. Zhao, R. Wang, F. Yang, L. Zhu, X. He, C. Li, Y. Jiang, Y. Jiang, M. Yang, M. Yang, Exploring the diagnostic value of photoacoustic imaging for breast cancer: the identification of regional photoacoustic signal differences of breast tumors, Biomed. Opt. Express 12 (Issue 3) (2021) 1407–1421, https://doi.org/10.1364/BOE.417056.

[27] R. Li, P. Wang, L. Lan, F.P. Lloyd, C.J. Goergen, S. Chen, J.-X. Cheng, J.-X. Cheng, Assessing breast tumor margin by multispectral photoacoustic tomography, Biomed. Opt. Express 6 (2015) 1273–1281, https://doi.org/10.1364/BOE.6.001273.

[28] I. Kosik, M. Brackstone, A. Kornecki, A. Chamson-Reig, P. Wong, M.H. Araghi, J.J.L. Carson, Intraoperative photoacoustic screening of breast cancer: a new perspective on malignancy visualization and surgical guidance, J. Biomed. Opt. 24 (2019) 1, https://doi.org/10.1117/1.JBO.24.5.056002.

[29] R. Nachabé, D.J. Evers, B.H.W. Hendriks, G.W. Lucassen, M. van der Voort, E.J. Rutgers, M.-J.V. Peeters, J.A. Van der Hage, H.S. Oldenburg, J. Wesseling, T.J.M. Ruers, Diagnosis of breast cancer using diffuse optical spectroscopy from 500 to 1600 nm: comparison of classification methods, J. Biomed. Opt. 16 (2011), 087010, https://doi.org/10.1117/1.3611010.

[30] K. Shen, S. Liu, T. Feng, J. Yuan, B. Zhu, C. Tian, Negativity artifacts in back-projection based photoacoustic tomography, J. Phys. D. Appl. Phys. 54 (2020), 074001, https://doi.org/10.1088/1361-6463/ABC37D.

[31] Y. Xu, L.V. Wang, G. Ambartsoumian, P. Kuchment, Reconstructions in limited-view thermoacoustic tomography, Med. Phys. 31 (2004) 724–733, https://doi.org/10.1118/1.1644531.

[32] G. Godefroy, B. Arnal, E. Bossy, Compensating for visibility artefacts in photoacoustic imaging with a deep learning approach providing prediction uncertainties, Photoacoustics 21 (2021), 100218, https://doi.org/10.1016/J.PACS.2020.100218.

[33] G. Diot, S. Metz, A. Noske, E. Liapis, B. Schroeder, S.V. Ovsepian, R. Meier, E. Rummeny, V. Ntziachristos, Multispectral optoacoustic tomography (MSOT) of human breast cancer, Clin. Cancer Res. 23 (2017) 6912–6922, https://doi.org/10.1158/1078-0432.CCR-16-3200.

[34] C. Lee, W. Choi, J. Kim, C. Kim, Three-dimensional clinical handheld photoacoustic/ultrasound scanner, Photoacoustics 18 (2020), 100173, https://doi.org/10.1016/J.PACS.2020.100173.

[35] Y. Zhou, S.V. Tripathi, I. Rosman, J. Ma, P. Hai, G.P. Linette, M.L. Council, R.C. Fields, L.V. Wang, L.A. Cornelius, Noninvasive determination of melanoma depth using a handheld photoacoustic probe, J. Invest. Dermatol. 137 (2017) 1370–1372, https://doi.org/10.1016/J.JID.2017.01.016.

[36] J. Aguirre, B. Hindelang, A. Berezhnoi, U. Darsow, F. Lauffer, K. Eyerich, T. Biedermann, V. Ntziachristos, Assessing Nailfold Microvascular Structure with Ultra-Wideband Raster-scan Optoacoustic Mesoscopy (2018), https://doi.org/10.1016/j.pacs.2018.02.002.

[37] B. Park, M. Han, J. Park, T. Kim, H. Ryu, Y. Seo, W.J. Kim, H.H. Kim, C. Kim, A photoacoustic finder fully integrated with a solid-state dye laser and transparent ultrasound transducer, Photoacoustics 23 (2021), 100290, https://doi.org/10.1016/J.PACS.2021.100290.

[38] B. Eddins, M.A.L. Bell, Design of a multifiber light delivery system for photoacoustic-guided surgery 22 (2017), https://doi.org/10.1117/1.JBO.22.4.041011.

[39] H. Kruit, K.J. Francis, E. Rascevska, S. Manohar, Annular fiber probe for interstitial illumination in photoacoustic guidance of radiofrequency ablation, Page 4458. 21 (2021), Sensors Vol. 21 (2021) 4458, https://doi.org/10.3390/S21134458.

[40] M.W. Schellenberg, H.K. Hunt, Hand-held optoacoustic imaging: a review, Photoacoustics 11 (2018) 14–27, https://doi.org/10.1016/J.PACS.2018.07.001.

[41] L.J. Griffiths, C.W. Jim, An alternative approach to linearly constrained adaptive beamforming, IEEE Trans. Antennas Propag. 30 (1982) 27–34, https://doi.org/10.1109/TAP.1982.1142739.

[42] B.T. Cox, B.E. Treeby, Effect of Sensor Directionality on Photoacoustic Imaging: A Study Using the k-Wave Toolbox, n.d. https://doi.org/10.1117/12.841671.

[43] P. Omidi, L.C.M. Yip, E. Rascevska, M. Diop, J.J.L. Carson, PATLAB: a graphical computational software package for photoacoustic computed tomography research, Photoacoustics 28 (2022), 100404, https://doi.org/10.1016/J.PACS.2022.100404.

[44] R. Nachabé, B.H.W. Hendriks, A.E. Desjardins, M. van der Voort, M.B. van der Mark, H.J.C.M. Sterenborg, Estimation of lipid and water concentrations in scattering media with diffuse optical spectroscopy from 900 to 1,600 nm, J. Biomed. Opt. 15 (2010), 037015, https://doi.org/10.1117/1.3454392.

[45] B. Treeby, B. Cox, J. Jaros, k-Wave A MATLAB toolbox for the time domain simulation of acoustic wave fields User Manual, n.d. http://www.k-wave.org/manual/k-wave_user_manual_1.0.1.pdf (accessed February 24, 2019).

[46] MATLAB - MathWorks - MATLAB & Simulink, (n.d.). https://nl.mathworks.com/products/matlab.html (accessed August 17, 2018).

[47] L.C.M. Yip, P. Omidi, E. Rascevska, J.J.L. Carson, Approaching closed spherical, full-view detection for photoacoustic tomography, J. Biomed. Opt. 27 (2022) 1–19, https://doi.org/10.1117/1.jbo.27.8.086004.

[48] ImageJ, (n.d.). https://imagej.nih.gov/ij/ (accessed October 7, 2021).

[49] 3D Slicer, (n.d.). https://www.slicer.org/ (accessed August 14, 2018).

[50] N. Azordegan, V. Fraser, K. Le, L.M. Hillyer, D.W.L. Ma, G. Fischer, M.H. Moghadasian, Carcinogenesis alters fatty acid profile in breast tissue, Mol. Cell. Biochem. 374 (2013) 223–233, https://doi.org/10.1007/S11010-012-1523-4.

[51] D. Jiang, H. Chen, Y. Shen, Y. Zhang, F. Gao, R. Zheng, F. Gao, Hand-held 3D Photoacoustic Imager with GPS, (n.d.).

[52] T.M. Allweis, Z. Kaufman, S. Lelcuk, I. Pappo, T. Karni, S. Schneebaum, R. Spector, A. Schindel, D. Hershko, M. Zilberman, J. Sayfan, Y. Berlin, A. Hadary, O. Olsha, H. Paran, M. Gutman, M. Carmon, A prospective, randomized, controlled, multicenter study of a real-time, intraoperative probe for positive margin detection in breast-conserving surgery, Am. J. Surg. 196 (2008) 483–489, https://doi.org/10.1016/J.AMJSURG.2008.06.024.

Elina Rascevska, MSc is a PhD candidate in Biomedical Engineering at Western University. She previously received her MSc degree in Biomedical Engineering from the University of Twente in 2019. Her research is focused towards the development of intraoperative photoacoustic imaging tools.

Lawrence C.M. Yip is a PhD candidate in Medical Biophysics at Western University, where he also received his Honours BMSc in Medical Sciences. His current research interests include system development of medical research devices with a focus on photoacoustic tomography and near-infrared spectroscopy. He is actively involved with the International Photoacoustic Standardisation Consortium.

Parsa Omidi, PhD is currently a Machine Learning Researcher at Huawei Technologies Canada Co., Ltd. He obtained his PhD in Biomedical Engineering from Western University in 2021. In addition, previous degrees include a MSc in Satellite Communication from the Iran University of Science and Technology and a BSc in Electronics from Isfahan University. He currently specialises in image and signal processing as well as in artificial intelligence.

Muriel Brackstone, MD, PhD, FRCSC is professor of Surgery and Oncology at Western University's Schulich School of Medicine Dentistry. She is a general surgeon with subspecialty fellowship training in breast surgical oncology. She initiated the Canadian locally advanced breast cancer consortium for national initiatives in advanced breast cancer treatment and is the lead author on a number of national clinical guideline documents for breast cancer care. Dr.Brackstone is the Medical Director of London's Breast Care Program and Director of the London Tumour Biobank. She has an interest in healthcare outcomes and clinical standards in breast surgery and maintains a comprehensive local clinical database from which patient treatment and outcomes can be evaluated.

Jeffrey J.L. Carson, PhD is a scientist at the Lawson Health Research Institute and an associate professor at Western University. He is an expert on optical imaging systems. His laboratory made early developments in snapshot 3D photoacoustic tomography, snapshot multispectral imaging, and photonic devices for optical imaging and sensing. He is cofounder of Spectral Devices Inc., which commercialized pixelated multispectral filter array technology originally developed in his laboratory.